Article

Enhancing the Fresh and Early Age Performances of Portland Cement Pastes via Sol-Gel Silica Coating of Metal Oxides (Bi$_2$O$_3$ and Gd$_2$O$_3$)

Krzysztof Cendrowski [1], Karol Federowicz [1], Mateusz Techman [1], Mehdi Chougan [2], Tomasz Kędzierski [3], Myroslav Sanytsky [4], Ewa Mijowska [3] and Pawel Sikora [1,*]

1   Faculty of Civil and Environmental Engineering, West Pomeranian University of Technology, 70-310 Szczecin, Poland; krzysztof.cendrowski@zut.edu.pl (K.C.); karol.federowicz@zut.edu.pl (K.F.); mateusz.techman@zut.edu.pl (M.T.)
2   Department of Civil and Environmental Engineering, Brunel University London, Uxbridge UB8 3PH, UK; mehdi.chougan2@brunel.ac.uk
3   Department of Nanomaterials Physicochemistry, Faculty of Chemical Technology and Engineering, West Pomeranian University of Technology, 70-310 Szczecin, Poland; tomasz.kedzierski@zut.edu.pl (T.K.); emijowska@zut.edu.pl (E.M.)
4   Department of Building Production, Lviv Polytechnic National University, 79-013 Lviv, Ukraine; myroslav.a.sanytskyi@lpnu.ua
*   Correspondence: pawel.sikora@zut.edu.pl

Abstract: Incorporating metal oxide nanoparticles into cement-based composites delays the hydration process and strength gain of cementitious composites. This study presents an approach toward improving the performance of bismuth oxide (Bi$_2$O$_3$) and gadolinium oxide (Gd$_2$O$_3$) particles in cementitious systems by synthesizing core–shell structures via a sol-gel process. Two types of silica coatings on cementitious pastes with 5% and 10% substitution levels were proposed. The rheology, hydration, and mechanical properties of the pastes were analyzed to determine the relationship between the coating type and nanoparticle concentration. The results indicate that despite the significant disparities in the performance of the resulting material, both methods are appropriate for cement technology applications. Bi$_2$O$_3$'s silica coatings accelerate the hydration process, leading to early strength development in the cement paste. However, due to the coarse particle size of Gd$_2$O$_3$, silica coatings exhibited negligible effects on the early age characteristics of cement pastes.

Keywords: cement paste; Bi$_2$O$_3$; Gd$_2$O$_3$; core–shell; rheology; sol-gel

1. Introduction

Heavy-weight microsized powders are widely used as additives to cementitious systems in construction and dental applications [1–4]. Due to their high atomic number, the replacement of Portland cement with microsized additives enables the production of composites with radiopacifying and radiation (gamma-ray and neutron) attenuation properties. In recent years, there has been growing concern regarding the production of lead-free materials; thus, various additives have been used, including Bi$_2$O$_3$, Ti$_2$O$_3$, WO$_3$, Gd$_2$O$_3$, and Fe$_3$O$_4$. Particular interest is placed on the application of Bi$_2$O$_3$ due to its high atomic number (Z = 83), low price, nontoxicity, and biocompatibility [5].

However, to ensure proper radiopacifying, radiation shielding characteristics of cementitious composites or a high-volume replacement of cement, which increases the density, or both, are needed. As heavy-weight metal oxide particles usually exhibit low affinity for the cement matrix, several problems occur in cementitious systems, including delayed hydration, retarded strength development, lower mechanical performance, and increased matrix porosity. Therefore, various mitigation techniques are sought to face and overcome these obstacles.

In recent years, there has been substantial interest in replacing conventional microsized additives with nanoparticles. Various studies confirmed that the addition of nanoparticles to various systems, e.g., polymeric matrices, improved radiation attenuation properties better than their microsized counterparts [6–8]. These effects are attributed to the unique surface properties as well as the smaller size of nanoparticles, resulting in better filling (packing) ability and more efficient distribution of the material within the matrix. To date, limited information on the inclusion of nanoparticles toward improving the radiation shielding and radiopacifying characteristics of cementitious systems is available.

Few experimental studies have reported the beneficial effects of the inclusion of nano-TiO_2 as a gamma-ray shielding concrete material; however, with higher dosages, a reduction in mechanical performance was observed [9–11]. Similar problems occurred with the addition of Fe_3O_4 nanoparticles [12,13]. Comparative studies on the effects of Bi_2O_3 powders confirmed the superior effects of nano-Bi_2O_3 compared to micro-Bi_2O_3 in cement-based applications in terms of radiation shielding properties [14–17]. In all available studies related to the inclusion of nano-Bi_2O_3, all cement-based composites exhibited lower mechanical performances than nonmodified (control) materials. As reported by Li and Coleman [3], the presence of the Bi_2O_3 powder delays the hydration process of cement, resulting in an increased setting time of cement pastes. However, when micro- and nanosized powders were compared, higher strength losses were reported for cement pastes containing microsized particles [15]. Thus, it can be concluded that nanoparticles can reduce the negative effect of a high content of additives to some extent.

The lower mechanical performance and slower strength development of cement-based composites containing nano-Bi_2O_3 is mainly attributed to its high-volume replacement rate with cement. To ensure proper radiation shielding characteristics, the addition of micro- or nanoparticles usually exceeds >5 wt% of binder [5,9–11,15–18]. In contrast, the State-of-the-Art recommended dosages of nanoparticles in cementitious systems, toward improving durability and mechanical characteristics, should usually not exceed 5 wt% of binder [19,20].

Both Bi_2O_3 and Gd_2O_3 are widely used as radiation-attenuating additives in other fields of materials science (e.g., polymers), while their performance in cement-based composites is not fully explored. Based on the abovementioned literature review, Bi_2O_3 nanoparticles possess a significant threat of having a dramatically delayed hydration process, which in turn can hinder or even prevent its use in prefabrication or 3D printing technology. Similarly, the effect of Gd_2O_3 powders on the performance of cement-based composites is extremely limited in the literature. Therefore, it is imperative to understand the performance of the abovementioned materials in the context of their potential application as radiation-attenuating additives for cementitious systems. This includes establishing relationships between their content on the fresh and hardened properties of cement-based composites as well as the potential development of potential mitigation methods for delayed hydration.

Researchers have explored various methods to increase the hydration rate and improve the embedding of nanomaterials within the cementitious matrix. One of the popular, inexpensive methods is the production of thin silica coatings on nanoparticle surfaces to increase their reactivity and improve their bonding with the matrix. Nanosized silica, due to its ultrafine size, high amorphicity, and remarkable reactivity, exhibits spectacular effects on accelerating the cement hydration process and improving the overall durability and mechanical properties of cement-based composites [21–24]. To date, various nanoparticles have been coated with silica layers, including Fe_3O_4 [25], TiO_2 [26], and carbon nanotubes [27,28]. Moreover, Pi et al. [29] proposed the production of nano-SiO_2-coated steel fibers for concrete applications.

To date, no information on research related to the early age characteristics of nano-Bi_2O_3-modified cement pastes is available. Moreover, no attempts to improve the performance of Bi_2O_3 nanoparticles with silica coatings were studied. Therefore, this study is the first to evaluate the possibilities of Bi_2O_3 nanoparticle coatings to improve the early

age performance of cement pastes containing such materials. Moreover, another potential neutron attenuator, Gd_2O_3 powder, was also coated with silica shells to evaluate the performance of coatings with different core materials.

2. Research Significance

To date, no studies related to the fresh and early age characteristics of cement pastes containing Bi_2O_3 and Gd_2O_3 powders are available. Moreover, no attempts to improve the performance of such materials by various silica coatings were studied in the literature. This study evaluates the effectiveness of radiation-attenuating additives (Bi_2O_3 and Gd_2O_3) in cement-based composites and explores methods for enhancing their performance in cement matrices. Therefore, two types of sol-gel silica coatings for the production of core–shell structures will be proposed for the first time, and their potential application in cementitious systems will be evaluated. Moreover, knowledge of Gd_2O_3 performance in cementitious systems will be evaluated, as only one study related to that field is available (to the best of the authors' knowledge). Therefore, this study will be the first to propose a comparative study on two types of sol-gel silica coatings for the synthesis of core–shell structures that can find application in cementitious systems. As an outcome, State-of-the-Art related to the effects of Bi_2O_3 and Gd_2O_3 on fresh and hardened properties will be extended, shedding new light on the potential use of the abovementioned materials for radiation shielding purposes. Moreover, new types of advanced additives will be proposed for potential radiation shielding applications.

3. Materials and Methods

3.1. Materials

Cement CEM I 42.5 R (Górażdże, Poland) and tap water conforming to EN 1008 were used to produce cement pastes. Bismuth oxide (Bi_2O_3) and gadolinium oxide (Gd_2O_3), with catalog numbers 637017 and 278513, respectively, were purchased from the Merck company. As a source of silica in the coating process, tetraethyl orthosilicate (TEOS) was purchased from the Merck company. Other chemical reagents, such as ethylene alcohol (ETOH) and 26% ammonium solution (NH_4OH), were purchased from Warchem (Trakt Brzeski, Poland). Figure 1 presents the particle size distribution (by volume) of materials used in this study determined using a laser diffraction method and a laser diffraction analyzer (Malvern Mastersizer 2000, Worcestershire, UK). The obtained curves confirm that both Bi_2O_3 and Gd_2O_3 powders are much finer than cement particles. However, a higher particle size was reported in Gd_2O_3 powder when compared to Bi_2O_3. The particle sizes of the powders will be discussed in detail in the Section 4.
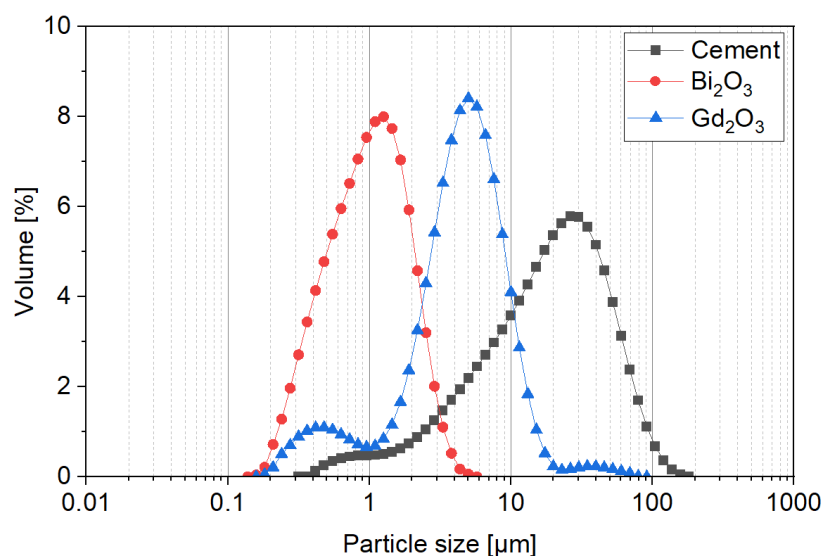

Figure 1. Particle size distribution (by volume) of dry materials used.

3.2. Metal Oxides Coatings with Silica Coatings

Metal oxide coating was performed using two different methods, which were designated as method A and method B, for better readability. Both methods are based on the Stöber method of synthesizing silica nanospheres [30].

In the first method (Figure 2A, method A), 100 mL ethylene alcohol (ETOH) was mixed with 2.5 mL of ammonium solution using a magnetic stirrer. After 1 h of mixing, 5 g of the metal oxide was alternatively dispersed in the obtained solution using a magnetic stirrer and ultrasound. After obtaining the suspension, the suspension was stirred using a magnetic stirrer. Next, 1.5 mL of TEOS was added to the flask. Furthermore, the suspension was stirred for 24 h at room temperature. In the last stage, the material was dried in air at 80 °C.

In the second method (Figure 2B, method B), 80 mL of distilled water and 20 mL of ETOH were poured into the flask and stirred using a magnetic stirrer. A total of 2.5 mL of ammonium solution was added to the stirred mixture of water and ETOH. Next, after 5 min, 1.5 mL of TEOS was added. The obtained solution was stirred for the next 24 h, with a stirrer rotation of 500 rpm. After stirring for 24 h, 5 g of metal oxide was added to the suspension and stirred for 60 min. Then, the suspension was cast on a flat surface, creating a thin, homogeneous layer. In the last stage, the cast suspension evaporated in the air at 90 °C for 24 h.
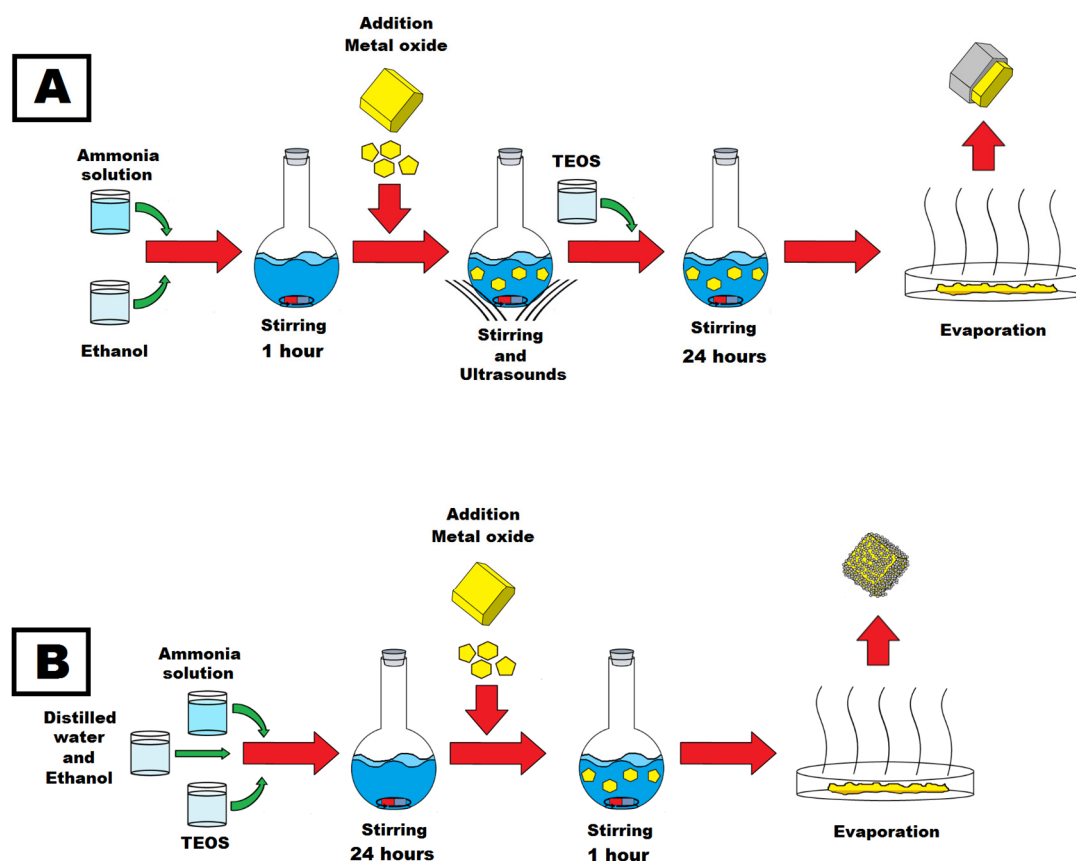

Figure 2. Scheme of the particle coating with the silica according to method-A (**A**) and method-B (**B**).

3.3. Cement Paste Mixture Design and Mixing Protocol

A set of 13 cement pastes was designed with a fixed water-to-cement (w/c) ratio of 0.4. The mix design of cement pastes is presented in Table 1. In nanomodified mixes, cement was replaced with particles at 5% and 10% (by weight). The control sample was designated as the control, while other mixes were designated following the method presented in Figure 3.

Table 1. Ratio of the cement paste components (wt%).

Sample Designation	Cement	Bi$_2$O$_3$	Gd$_2$O$_3$	Bi$_2$O$_3$-A	Bi$_2$O$_3$-B	Gd$_2$O$_3$-A	Gd$_2$O$_3$-B	Water
Control	1	-	-	-	-	-	-	0.4
Bi5	0.95	0.05	-	-	-	-	-	0.4
Bi5A	0.95	-	-	0.05	-	-	-	0.4
Bi5B	0.95	-	-	-	0.05	-	-	0.4
Bi10	0.90	0.10	-	-	-	-	-	0.4
Bi10A	0.90	-	-	0.10	-	-	-	0.4
Bi10B	0.90	-	-	-	0.10	-	-	0.4
Gd5	0.95	-	0.05	-	-	-	-	0.4
Gd5A	0.95	-	-	-	-	0.05	-	0.4
Gd5B	0.95	-	-	-	-	-	0.05	0.4
Gd10	0.90	-	0.10	-	-	-	-	0.4
Gd10A	0.90	-	-	-	-	0.10	-	0.4
Gd10B	0.90	-	-	-	-	--	0.10	0.4

Type of metal oxide:
Bi: Bi$_2$O$_3$
Gg: Gd$_2$O$_3$

Bi 10 A

Coating method:
blank: no coating (pristine)
A: coating – Method A
B: coating – Method B

Cement replacement level:
5: 5 wt%
10: 10 wt%
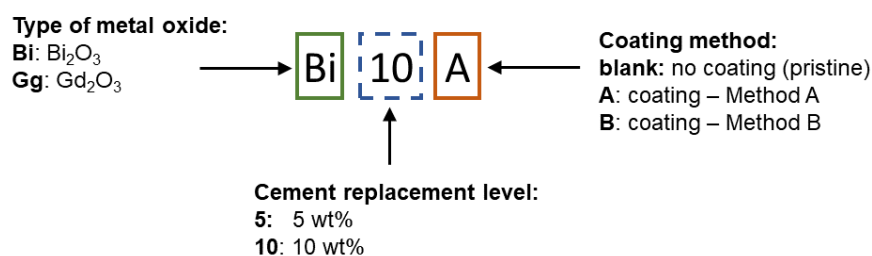
Figure 3. Schematic representation of sample designation.

Cement pastes were mixed using an automatic hand mixer. In the first stage, the mixture of (tap) water and nanoparticles was ultrasonicated for 10 min using an ultrasonic bath. The solution was mixed with cement following the procedure: (i) 30 s slow mixing, (ii) 60 s fast mixing, (iii) 30 s rest, and (iv) 60 s fast mixing. Mixed samples were cast into 20 × 20 × 20 mm molds, covered in foil, and cured at room temperature for 24 h (T = 20 °C ± 1 °C). Afterward, cubes were de-molded and stored in the container up to 28 d with RH = 95% and T = 20 °C ± 1 °C.

3.4. Testing Methodology

An Aeris diffractometer (Malvern Panalytical, Malvern, UK) with Cu-Kα radiation (λ = 1.544 Å) was used to analyze the crystallinity and phase composition of the nanomaterials. Transmission electron microscopy (TEM, Tecnai F30 with a field emission gun operating at 200 kV, Thermo Fisher Scientific, Waltham, MA, USA) with energy dispersive X-ray spectroscopy (EDS) was used to evaluate the morphology and composition of the samples. The specific surface area was measured using an N$_2$ adsorption/desorption isotherm (Micromeritics ASAP 2460, Norcross, GA, USA).

The heat evolution rate of cement pastes was determined using a TAM-Air (TA Instruments, Waters, Wakefield, MA, USA) isothermal calorimeter. A total of 12.6 g of paste (9 g binder + 3.6 g water/solution) was mixed externally using a vibration mixer and put immediately inside the calorimeter. The rate of hydration was measured up to 168 h.

The consistency of cement pastes was determined using a mini-slump test. After mixing, the cement pastes were poured into a mini-flow cone. A mini cone (Figure S1, Supplementary Materials) with a top diameter, bottom diameter, and height of 36, 60, and 60 mm, respectively, was used [31]. Afterward, the cone was raised vertically, and 15 hits to the flow table were applied. The spread flow (mean diameter) was determined in two perpendicular directions, and the mean value was taken as a representative.

The rheological parameters of the cement pastes were measured using a Rheotest RN4 rotational rheometer with concentric cylinder geometry. Cement pastes were tested 5 min after water/cement contact. The rheology test was conducted using a modified version of

the [32] methodology. The mixture was initially pre-sheared for 30 s at a constant shear rate of 100 s^{-1}. The shear stress of the mixtures was then calculated for a total of 300 s at 20 points distributed uniformly along a logarithmic scale, with shear rates ranging from 100 s^{-1} to 0.1 s^{-1}. In this study, the yield shear stress (τ_0) and plastic viscosity (η_p) of each mixture were determined using the modified Bingham model (MBM). The Herschel–Bulkley model, the Bingham model, and the modified Bingham model are examples of fitting models that have been described for the rheological assessment of cementitious composites. The MBM approach (Equation (1)) was chosen to address the non-Newtonian and pseudoplastic behavior of cementitious composites and achieve better fitting accuracy.

$$\tau = \tau_0 + \eta_P \gamma + c\gamma^2 \tag{1}$$

where c is a constant, τ is the shear stress, τ_0 is the yield shear stress, η_p is the plastic viscosity, and γ is the shear rate.

The compressive strength of the cement pastes was determined after 1 d, 2 d, 7 d, and 28 d of curing using a UNIFRAME 250 electromechanical universal tester (CONTROLS S.p.A., Liscate, Italy) with a loading rate of 0.6 MPa/s. Three samples of each type of composite were tested, and the mean value was taken as representative.

3.5. Nanomaterials Physical and Chemical Characterization Techniques

The morphology of the materials before and after coating was examined with a transmission electron microscope (TEM, Tecnai G2 F20 S-TWIN, FEI). Additionally, TEM was equipped with a high-angle annular dark field HAADF detector (STEM) and X-ray energy dispersive spectroscopy (EDAX) module for elemental distribution analysis. The chemical composition of the samples was analyzed using an energy-dispersive X-ray fluorescence spectrometer (Epsilon3) and X-ray powder diffractometer (Aeris, Malvern Panalytical, Malvern, UK) with an accelerating voltage of 40 kV and a tube current of 7.5 mA. Cu-Kα radiation (λ = 1.544 Å) was used as an excitation source. Additionally, the chemical composition of the synthesized silica coatings was analyzed with a Raman microscope (Renishaw, New Mills Wotton-under-Edge, UK) with an excitation wavelength of 785 nm. The images of silica coatings were taken using a Delta Optical microscope (Delta Optical, SZ-430B, Mississauga, ON, Canada) equipped with a 20 MP camera (DLT-Cam PRO). N$_2$ adsorption/desorption isotherms were acquired using Micromeritics ASAP 2460. The surface area, pore volume, and median were calculated according to the Brunauer–Emmett–Teller (BET) and DFT methods, respectively.

4. Results and Discussion

4.1. Nanomaterials Characterization

The XRD analysis of the bismuth and gadolinium oxides before and after silica coating is presented in Figure 4. The bismuth oxide spectrum (Figure 4A) before and after silica coating (via method A or method B) shows the same peak positions with similar intensities. Peaks from Bi$_2$O$_3$ can be assigned to the β-Bi$_2$O$_3$ phase, according to PDF 27-0050. No additional peaks other than those assigned to pristine Bi$_2$O$_3$ were identified. The gadolinium oxide patterns before (Gd$_2$O$_3$) and after silica coating (via method A or method B) are similar in terms of peak position and intensity (Figure 4B). The peaks in the XRD pattern of Gd$_2$O$_3$ can be assigned according to JCPDS card no. 43-1014. According to the X-ray fluorescence (XRF) analysis, the contents of silica in the Bi$_2$O$_3$ and Gd$_2$O$_3$ coated via method A and method B are 6.84%, 6.68%, 6.98%, and 6.80%, respectively. The XRD results confirm that the synthesis of silica coatings did not influence the chemical structure of the metal oxide core.

A schematic representation of the synthesis process of silica coatings on Bi$_2$O$_3$ is presented in Figure 5A. The TEM images of pristine bismuth oxide (Figure 5B,C) show a spherical structure with a diameter ranging from 93 nm to 643 nm. The mean diameter of the pristine Bi$_2$O$_3$ particles is 250 nm. The surface of the particles is smooth and free from impurities. The high-magnification images of the Bi$_2$O$_3$ particles show lattice planes,

proving the crystal structure of the metal oxide particles. TEM images of the lattice planes are presented in Figure S2A (Supplementary Materials). Bismuth oxide particles coated with silica according to method A are presented in Figure 5D,E. The images show a solid silica coating over the bismuth oxide core. The thickness of the silica shell ranges from 26 nm up to 35 nm, with a mean thickness of approximately 30 nm. The thickness of the silica shell was estimated by TEM image analysis.
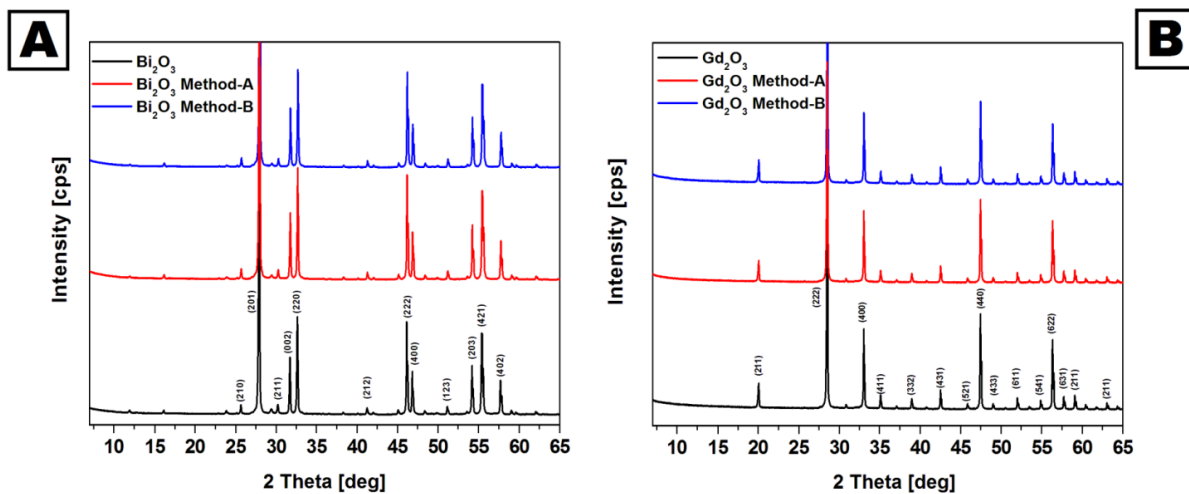

Figure 4. XRD spectra of the Bi_2O_3 (**A**) and Gd_2O_3 (**B**) before and after coating with the silica.
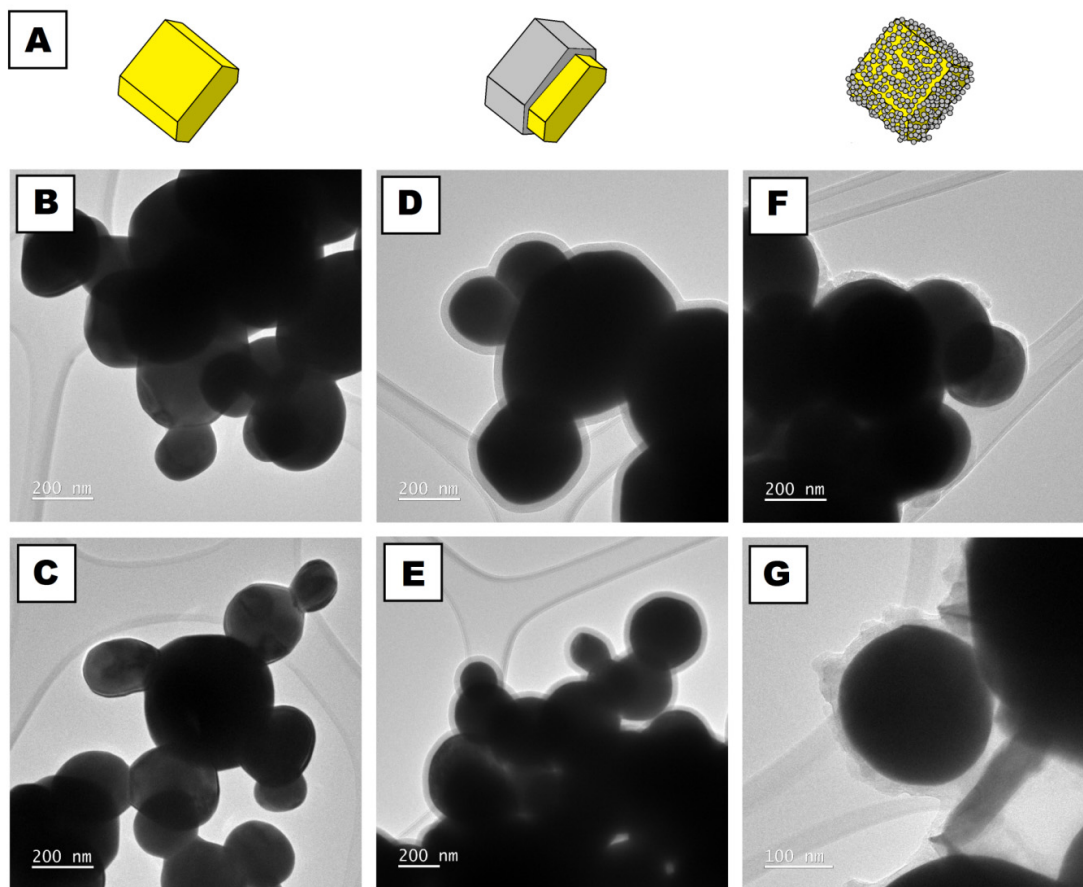

Figure 5. Graphical representation of the Bi_2O_3 particle before and after coating with silica according to method A and method B (**A**). TEM images of Bi_2O_3 before (**B**,**C**) and after coating with silica via method A (**D**,**E**) and method B (**F**,**G**).

TEM images of the bismuth oxide particles coated with silica via method B are presented in Figure 5F,G. The silica coating exhibits an irregular shape. Depending on the spot on the particle, the thickness of the silica coating size varies from 10 nm to 47 nm. In some spots, metal oxide cores may lack any coating. The structure of silica synthesized via method B (without cores) is presented in Figure S3 (Supplementary Materials). It is composed of silica particles with sizes below 15 nm. Due to this, silica coatings can show increased surface area by pore formation between the particles. The structures of the silica coatings, synthesized according to method A, were previously reported [33]. Previous studies showed that silica coatings, via method A, have a solid structure. It was proven by the slight increase in the surface area of the iron oxide after coating with silica. The surface area increased from 52 m^2/g to 60 m^2/g, compared to 117 m^2/g obtained with the mesoporous silica coating. Second, the solid structure of the silica coatings increased the chemical resistance of the cores due to acid etching. After coating with a thin silica layer of 20 nm, iron oxide nanoparticles prevented the dissolution of iron with hydrochloric acid [33].

Energy-dispersive X-ray spectroscopy (EDS) was used to analyze the elemental distribution of the pristine and silica-coated bismuth oxide particles. The maps of the distribution of bismuth, oxygen, and silica are presented in Figure 6. The images taken using scanning transmission electron microscopy (STEM) of the analyzed structure are presented in the Supplementary Materials (Figure S4A–C). The EDS of pristine Bi_2O_3 shows that signals from bismuth and oxygen correspond to each other, proving that the structure is composed of bismuth oxide. After the silica coating Bi_2O_3, the silica signal mostly corresponds to the signal from oxygen. In comparison with the signal from bismuth, it is clearly visible that the signal from silica is located on the outer layer of the structure, whereas the bismuth signal is located throughout the structure. The EDS analysis proves the successful silica coating of Bi_2O_3, regardless of the chosen silica coating method.
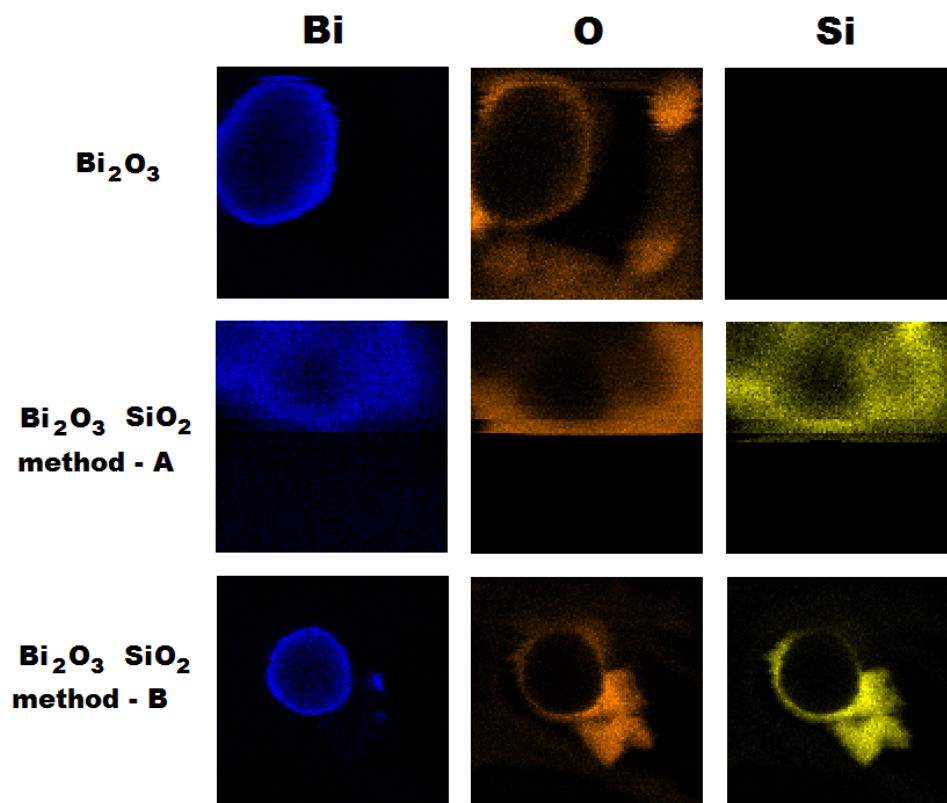

Figure 6. EDS mapping of bismuth, oxygen, and silica in pristine Bi_2O_3, and Bi_2O_3 after coating with silica via method-A and method-B.

　　　　A schematic representation of the synthesis process of silica coatings on Gd_2O_3 is presented in Figure 7A. According to the TEM images, pristine gadolinium oxide structures (Figure 7B,C) are composed of agglomerates of small crystals (from 101 nm to 248 nm) with more spherical and regular shapes. The size and shape of the Gd_2O_3 agglomerates are more irregular, with sizes measured in micrometers (from 256 nm to 2000 nm). Similar to Bi_2O_3 particles, Gd_2O_3 particles in high-magnification images show lattice planes, proving their crystal structure (Figure S2B, Supplementary Materials). The surface of the Gd_2O_3 microparticles is smooth in comparison to gadolinium oxide particles coated with silica according to method A. TEM images of the coated microparticles are presented in Figure 7D,E. The TEM images show solid silica coating over the Gd_2O_3 core, with thicknesses from 14 nm to 38 nm. The mean thickness around the Gd_2O_3 core is approximately −23 nm. The thickness of the silica shell was estimated based on TEM image analysis.
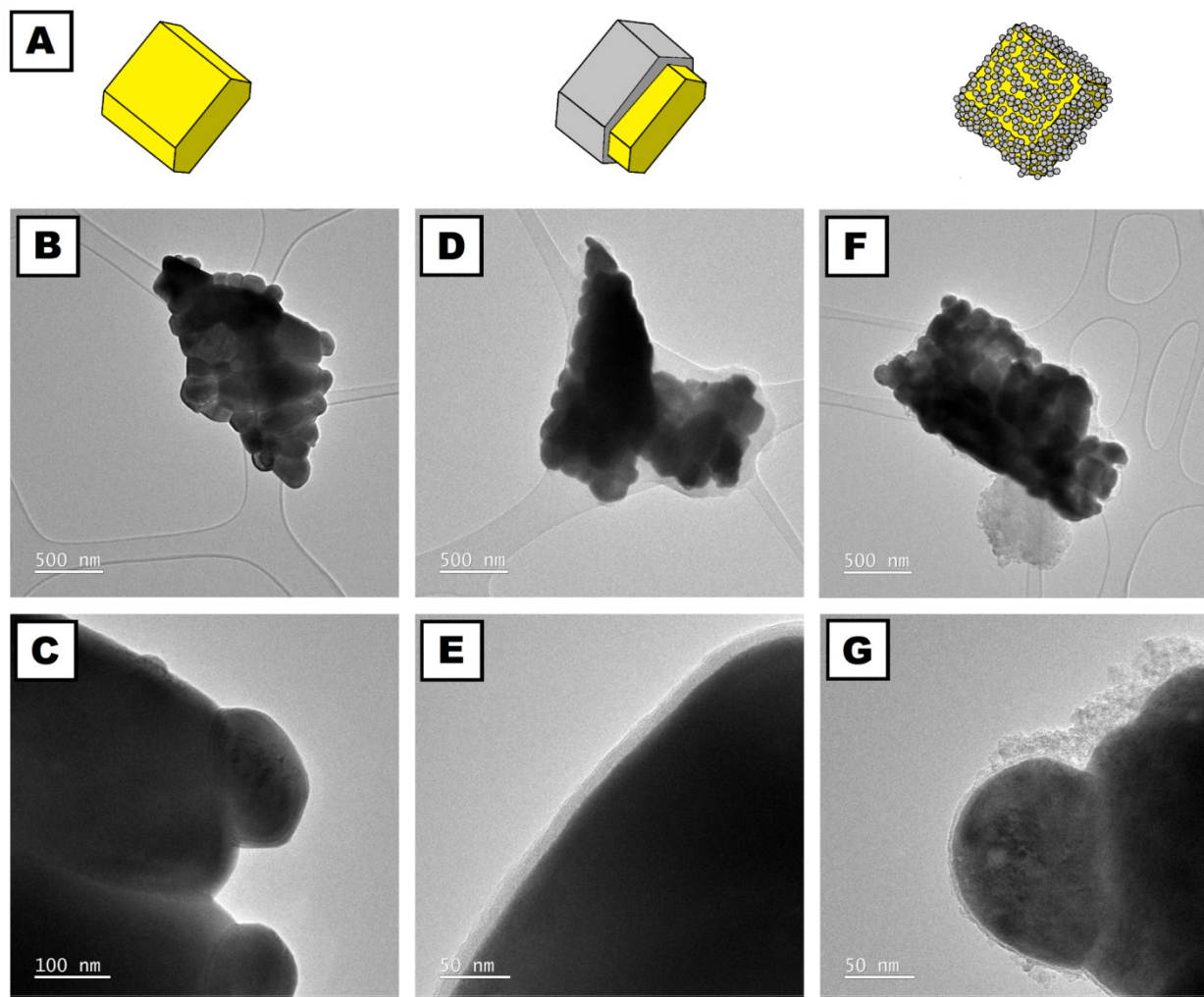

Figure 7. Graphical representation of the Gd_2O_3 particle before and after coating with silica according to method A and method B (**A**). TEM images of Gd_2O_3 before (**B,C**) and after coating with silica via method A (**D,E**) and method B (**F,G**).

　　　　Similar to bismuth oxide, gadolinium oxide microparticles coated with silica via the second method have irregular shapes and sizes (Figure 7F,G). The thickness of the silica coating differs depending on the spot on the microparticles. In some spots, metal oxide microparticles are uncoated or stuck to each other with silica coating. The thickness of the silica coating ranges from 5 nm to 40 nm. The mean diameter of the silica coating is approximately 17 nm.

To prove the silica coating, EDS mapping of selected elements of pristine and silica-coated gadolinium oxide particles is presented in Figure 8. The EDS of pristine Gd_2O_3 shows that the signals from gadolinium and oxygen correspond to each other. This proves that the structure is composed of gadolinium oxide and is free from silica. After the silica coating of Gd_2O_3, the signal from silica mostly corresponds to the signal from oxygen. In comparison to the signal from gadolinium, it is clearly visible that the signal from silica is located on the outer layer of the structure, whereas the gadolinium signal is located throughout the structure. The EDS analysis proves successful silica coating of the Gd_2O_3, regardless of the method of silica coating.
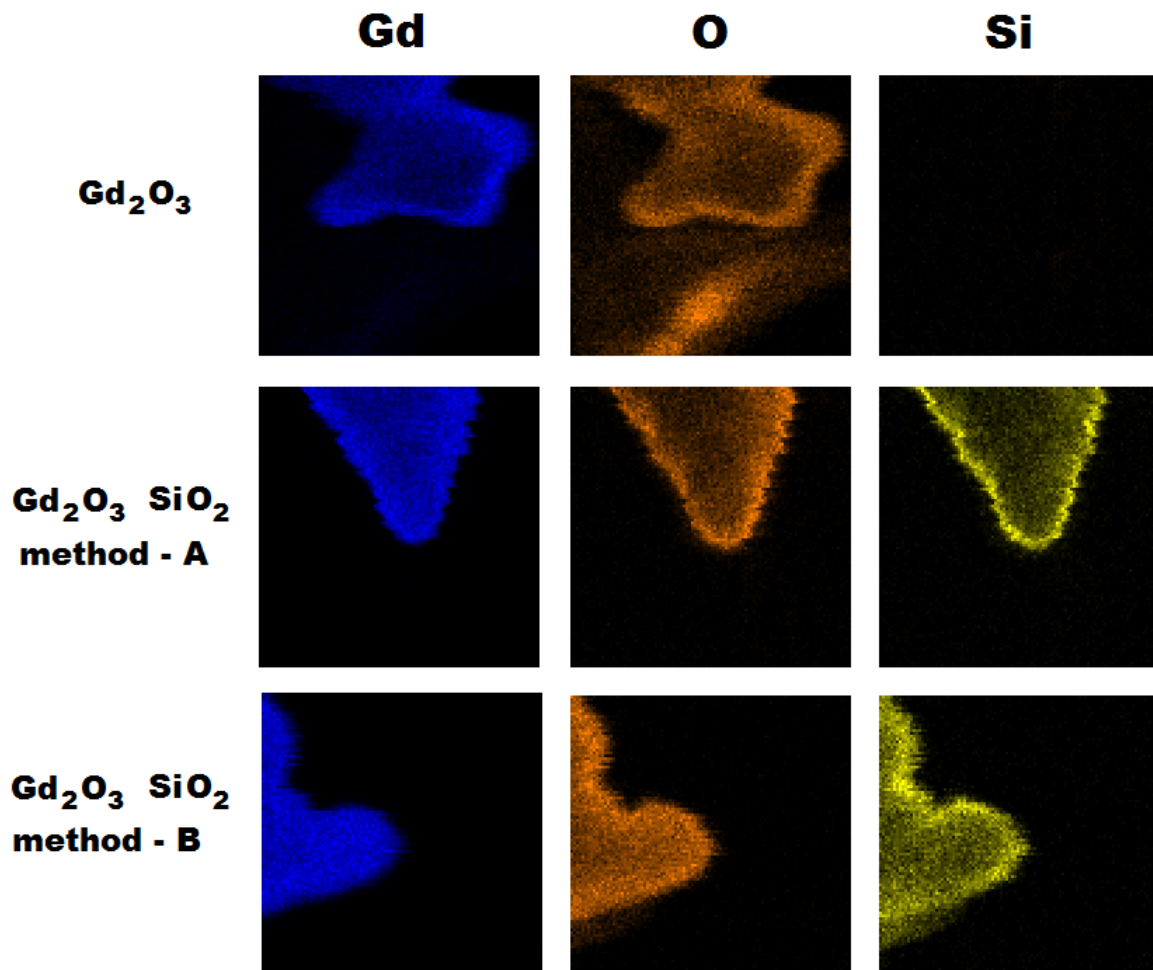

Figure 8. EDS mapping of gadolinium, oxygen, and silica in pristine Gd_2O_3, and Gd_2O_3 after coating with silica via method-A and method-B.

BET surface analysis proves the successful coating of bismuth and gadolinium oxides with silica. Bismuth oxide coating with method A resulted in an increase in the metal oxide surface area from 1.1007 cm^2/g to 3.429 cm^2/g. The surface area of the bismuth oxide coated using method B resulted in a significant increase in the surface area up to 81.3 cm^2/g. Similar to Bi_2O_3, coating of gadolinium oxide with method A resulted in an increase in the surface area from 0.1666 cm^2/g to 18.3015 cm^2/g, while coating with method B resulted in an increase in the surface area up to 87.22 cm^2/g. All surface areas and pore size/volume data are summarized in Table 2.

Table 2. Surface area and pore volume.

Sample	BET Surface Area [cm^2/g]	DFT Median Pore Width [Å]	DFT Total Volume in Pores [cm^3/g]
Bi_2O_3	1.1007	9.116	0.00042
Bi_2O_3 method-A	3.429	6.658	0.00091
Bi_2O_3 method-B	81.3367	11.626	0.05473
Gd_2O_3	0.1666	7.551	0.00007
Gd_2O_3 method-A	18.3015	10.718	0.00025
Gd_2O_3 method-B	87.220	11.859	0.08523

The metal oxide particles were successfully coated with silica coatings via two methods. Depending on the method of silica coating, different coating structures and thicknesses were obtained. Core particles coated with silica via the first method (method A) resulted in the formation of a solid shell with regular thickness. The silica shell synthesized via the second method (method B) had an irregular thickness and porous structure. Both silica coatings increased the surface area and pore volume. The increase in the surface area can be explained by the lower density of the silica coatings in comparison to that of the metal oxide core. Changes in the surface area are also related to the structure of the silica coatings. According to the TEM analysis, the silica coating forms a solid layer (method A) or a porous layer is formed from small particles (method B). The formation of the porous structure is proven by the higher total volume in pores (Table 2).

The silica shell synthesized via method B, except for the higher porosity and surface area, has a second advantage over method A in terms of the requirements and complexity of synthesis. For the synthesis of SiO_2 via method B, 80% of ethanol is replaced with distilled water, which reduces the synthesis costs. Another advantage of the synthesis of silica shells using method B is the following two-step synthesis: (i) silica precursor hydrolysis and condensation and (ii) formation of silica shells. Separate stages of silica shell formation from silica precursor hydrolyses and condensation allow simultaneous preparation of solutions of hydrolyzed and condensated TEOS and metal oxide core coating by evaporation of the TEOS solution. During the synthesis of the silica shell via method A, both processes co-occur during stirring in the glass beaker. Simultaneously, TEOS hydrolysis/condensation and shell formation do not speed up the whole process since the metal oxide cores require proper homogenization in the solution. Achieving a homogeneous solution requires stirring and sonication. It complicates and increases the costs of silica synthesis. Both methods require the separation of the coated cores from the solution in the last step. In method A, the process of nanomaterial separation can be selected from filtration, centrifugation, or evaporation [34]. However, in method B, it is necessary to evaporate the solution since it is necessary for silica precursor condensation.

Silica nanomaterials synthesized according to method A and method B also differ in terms of post-synthetic solutions and structure of the obtained materials (Figure S4A, Supplementary Materials). The difference in the structures of the as-synthesized silica materials is clearly noticeable in the microscope images (Figure 9). Optical microscopic analysis of the silica synthesized according to method A showed a white color and powder form (Figure 9A–C). This microscopic analysis is in accordance with previous studies on the synthesis of silica nanomaterials (spheres, coatings) [33–35]. According to previous studies, silica synthesized via method A has a nonporous, amorphous character [35].

Microscopic analysis of the silica synthesized according to method B (Figure 9D–F) shows that the synthesized silica has a crystal form resembling glass. Images D and E show transparent pieces of dried silica. White spots on the transparent pieces are microsized silica from the crushed, broken, or grounded silica pieces. Figure 9F shows an image of the small white particles at higher magnification. This image proves that white particles have a similar structure/form to the macrosized silica pieces.
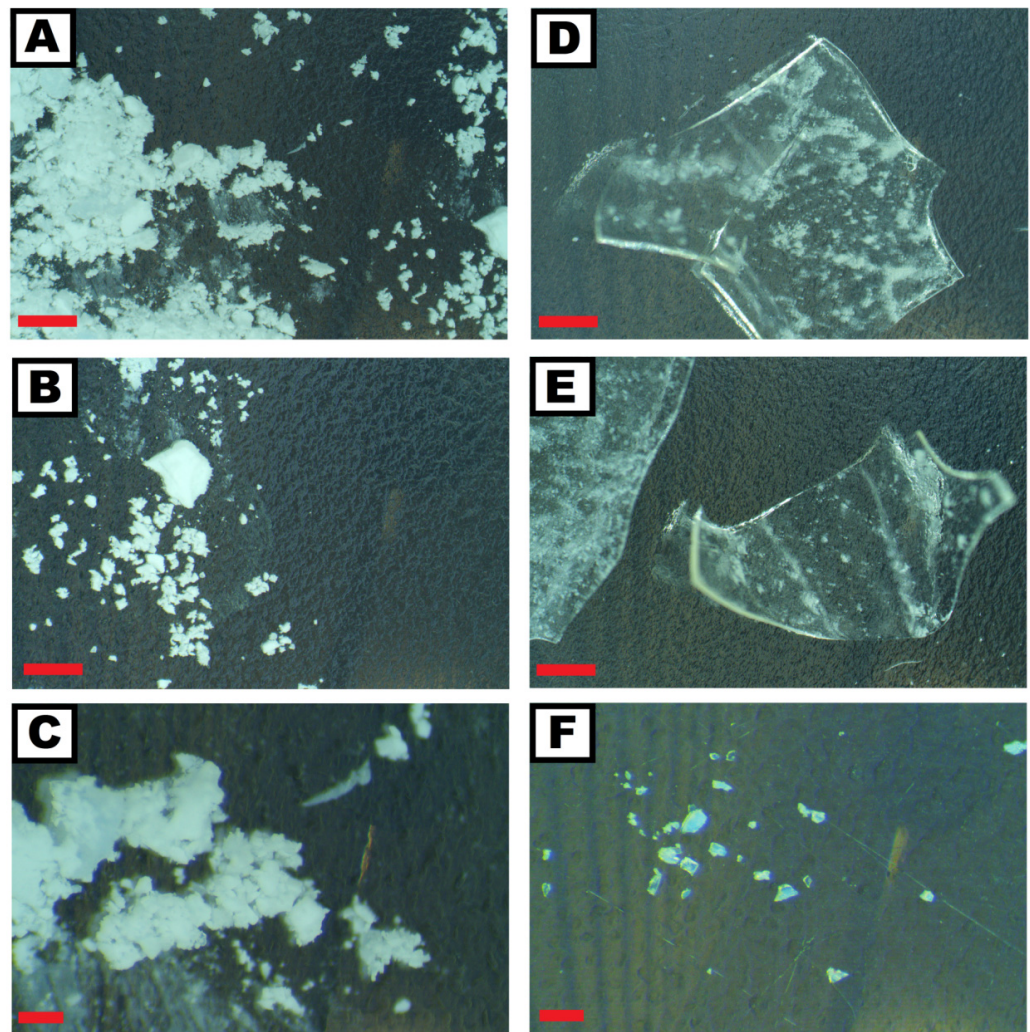
Figure 9. Microscopic images of the silica synthesized via method A (**A**–**C**) and method B (**D**–**F**). The scale for images (**A,B,D,E**) represents 1 mm (red line). The scale for images (**C,F**) corresponds to 0.2 mm (red line).

Between both samples, a clear difference can be noticed during their synthesis (Figure S4B,C, Supplementary Materials). A solution from the synthesis silica according to method A changes from transparent and colorless to milky white (Figure S4B, Supplementary Materials). The solution after synthesis of silica via method B remained transparent and colorless (Figure S4C, Supplementary Materials). A previous study performed by Kyong Ku Yun et al. shows that depending on the size, the color of the silica suspensions differs [36]. As reported, silica up to 30 nm shows a tendency to create transparent solutions. A further increase in the size of colloidal silica changes the color to white and milky white. Their studies are in accordance with our present and previous studies on nanosilica.

Raman analysis of both silica materials did not show significant changes between samples (Figure S5, Supplementary Materials). It suggests that silica materials have amorphous structures. Raman data, along with the optical microscope analysis, suggest that silica synthesized via method B can be classified as fused silica. Fused silica is characterized by high purity, silica particles below 15 nm, chemical resistance, a cross-linked 3D structure, and deep ultraviolet transparency [37]. It resembles quartz due to the regular arrangement of molecules only in local areas of density. In these organized domains or clusters, silicon oxide anions are somehow mutually oriented at short distances.

4.2. Isothermal Calorimetry

Figure 10 presents heat flow and cumulative heat curves for cement pastes containing Bi_2O_3 and Gd_2O_3 particles. A remarkable delay in the hydration process of cement pastes containing pristine Bi_2O_3 nanoparticles is visible (Figure 10A,B). The occurrence of a second hydration peak was delayed by 73% and 132%, and the magnitude of the peak decreased by 30% and 38% for Bi5 and Bi10, respectively, when compared to the control (Table 3). Similarly, the cumulative heat release in the first 24 h of Bi5 and Bi10 was markedly decreased (approximately by half) when compared to the control (Table 4), which had a substantial effect on strength development in the first day of hydration (Section 4.4). After 168 h, the cumulative heat values of Bi5 and Bi10 were lower by 6% and 11%, respectively, which can be directly related to the replacement level of cement with Bi_2O_3 particles. Therefore, it can be concluded that Bi_2O_3 nanoparticles have a substantial effect on delaying the hydration process, especially in the first 48 h of the hydration process.
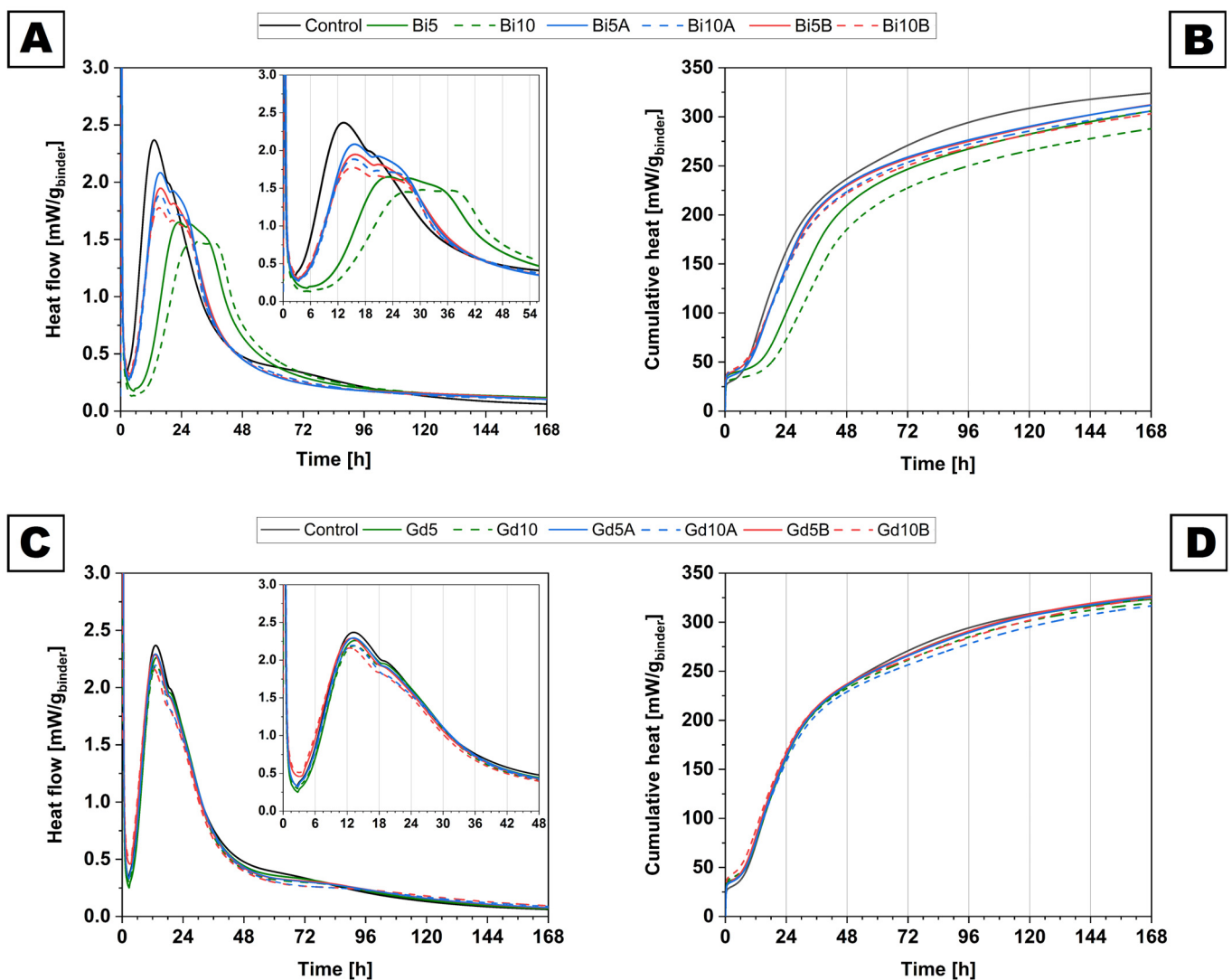

Figure 10. Heat flow (**A**,**C**) and cumulative heat (**B**,**D**) curves (per gram of binder) of cement pastes.

To date, no studies related to the hydration mechanisms of cement pastes containing nanosized Bi_2O_3 are available. As reported by Grazziotin-Soares et al. [1], cementitious systems containing a replacement rate of 20 wt% with Bi_2O_3 micropowder exhibited noticeably delayed initial and final setting times. A calorimetric study performed by Li and Coleman [3] confirmed that a cementitious system containing 20 wt% cement replacement with microsized Bi_2O_3 delayed the occurrence of a second exothermic peak from 8 h 47 min

(power of 9.09 mW/g^{-1}) to 11 h 7 min (power of 6.65 mW/g^{-1}). Therefore, based on the results presented in our study, it can be concluded that Bi_2O_3 nanoparticles have a much more marked effect on delaying the hydration process than microsized powders.

Table 3. Maximum exothermic heat rate and peak occurrence.

Sample Designation	Maximum Heat Flow [mW/g]	Loss/Rise in Comparison to Control [%]	Peak Occurrence [h]	Loss/Rise in Comparison to Control [%]
Control	2.37	-	12 h 54 min	
Bi5	1.65	−30	22 h 21 min	−73
Bi5A	2.08	−12	15 h 03 min	−17
Bi5B	1.95	−18	15 h 24 min	−19
Bi10	1.48	−38	29 h 53 min	−132
Bi10A	1.88	−21	14 h 45 min	−14
Bi10B	1.78	−25	15 h 02 min	−17
Gd5	2.26	−5	13 h 03 min	−1
Gd5A	2.29	−3	12 h 39 min	+2
Gd5B	2.29	−3	11 h 15 min	+13
Gd10	2.19	−8	13 h 00 min	−1
Gd10A	2.20	−7	12 h 57 min	0
Gd10B	2.16	−8	12 h 02 min	+7

Table 4. Percentage (%) of cumulative heat at selected time intervals compared to the control sample.

Sample Designation	12 h	24 h	36 h	48 h	72 h	168 h
Control	-	-	-	-	-	-
Bi5	64	61	79	88	91	94
Bi5A	85	90	97	98	96	96
Bi5B	90	90	96	97	95	96
Bi10	52	45	64	78	84	89
Bi10A	89	88	94	94	94	94
Bi10B	94	88	93	94	92	94
Gd5	102	100	100	99	98	100
Gd5A	105	100	100	100	98	100
Gd5B	111	102	101	100	99	101
Gd10	106	100	99	98	97	99
Gd10A	104	97	98	97	95	98
Gd10B	120	104	101	100	97	100

Coating Bi_2O_3 with silica layers resulted in a spectacular acceleration of the hydration process of cementitious systems and, thus, a substantial reduction in the negative impact of pristine Bi_2O_3 (Figure 10). Coating with method A was more effective in reducing the negative impact of the presence of Bi_2O_3 in the system. The occurrence of a second exothermic peak was delayed by only 17% and 14% in the Bi5A and Bi10A groups, respectively, when compared to the control. A slightly longer delay of peak occurrence by 19% and 17% (respectively) was reported for samples Bi5B and Bi10B (Table 3) when compared to the control. Similarly, the maximum heat rates reached by samples produced with silica-coated Bi_2O_3 were increased when compared to cement pastes containing pristine Bi_2O_3. Moreover, a remarkable rise in early cumulative heat release in samples containing Bi_2O_3 coated with silica was observed when compared to pastes containing pristine Bi5 and Bi10 (Table 4). It was confirmed by the early mechanical performance of cement pastes (Section 4.4). It is worth noting that from 36 h of hydration, the total released heat values were only slightly lower than the value of the control sample (Table 4). Therefore, the presence of silica coatings on the surface of Bi_2O_3 particles has a marked effect on accelerating the hydration process and reducing the negative impact of pristine Bi_2O_3, especially in the first two days of the hydration process.

The introduction of Gd_2O_3 particles (Figure 10C,D) into the cementitious system did not remarkably affect the hydration process, as in the case of Bi_2O_3 nanoparticles. In all cases (Gd5 and Gd10), the delay in the hydration process, as well as the decrease in the peak magnitude, did not exceed 10% (Table 3) when compared to the control. Similarly, the total heat releases up to 168 h of samples Gd5 and Gd10 were comparable to the value of the control paste (Table 4). To date, limited literature is available on the hydration process of cementitious systems containing Gd_2O_3 powders. However, a study by Piotrowski et al. [38] confirmed that composites with higher Gd_2O_3 dosages (up to 10 wt%) act as a slight retarder of the cement hydration process but accelerate aluminate activity. The coating of Gd_2O_3 with a silica shell had a marginal effect on the performance of the material when compared to nanosized Bi_2O_3. It can be attributed to the coarser particle size of Gd_2O_3 compared to Bi_2O_3 (Figure 1) and, thus, the lower reactivity of the material in the cementitious system. As reported in Section 4.1, the Gd_2O_3 used in this study is an agglomerated material composed of nanosized crystals; thus, its potential filling and seeding ability is limited. Therefore, the silicon coatings, regardless of their type, exhibited marginal effects on the cement hydration process. However, in the first 12 h of hydration, slightly higher rates of heat release were reported only for cement pastes containing Gd_2O_3 particles coated with type B silica (Table 4).

Therefore, based on the observed results, it can be concluded that the proposed silica coatings, regardless of coating type, have a marked effect on accelerating the hydration process of Bi_2O_3 nanoparticles, while its efficiency is decreased in coarser Gd_2O_3 particles. The discrepancy between coating methods that favor the method A coating could be associated with a higher amorphicity level of the solid silica shell as a result of the synthesis process, despite having a substantially lower surface area (Table 2).

4.3. Fresh Property Evaluations

The flow curves, i.e., shear stress versus shear rate, of all the mixtures with and without binder replacement materials are shown in Figure 11A,B. From the flow curves, the flowability characteristics, yield shear stress (τ_0), and plastic viscosity (η_p) were determined (Table 5). The mixtures' flow behavior (see Figure 11C) with and without heavy-weight components was assessed to evaluate the mix's consistency by employing the mini-cone test.

Table 5. Rheological parameters of cement pastes were determined using the MB model.

| Sample Designation	Yield Shear Stress	Plastic Viscosity	R^2
Control	7.16222	1.02845	0.99699
Bi5	8.74182	1.05081	0.99751
Bi5A	11.64369	1.15427	0.98882
Bi5B	7.16222	1.02845	0.99699
Bi10	7.36615	1.29074	0.99607
Bi10A	7.26896	1.32779	0.99714
Bi10B	10.69441	1.1534	0.99625
Gd5	6.4069	1.15999	0.99733
Gd5A	9.23405	1.04431	0.99651
Gd5B	10.26487	1.2161	0.99756
Gd10	9.90964	1.01193	0.99845
Gd10A	3.41433	1.13131	0.99798
Gd10B	4.46031	1.90798	0.99107
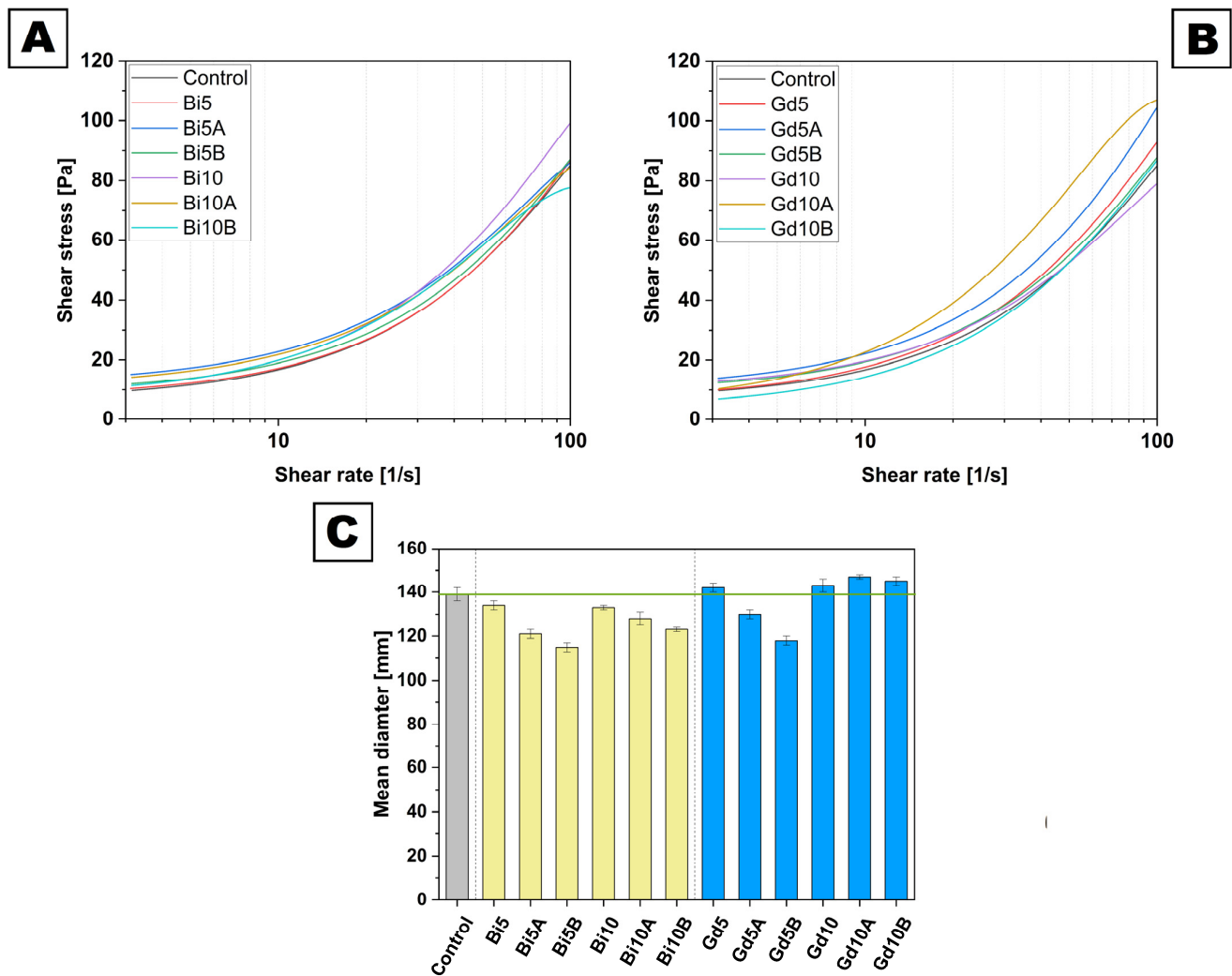
Figure 11. Rheology test results for mixtures containing bismuth oxide particles (**A**). Gadolinium oxide particles (**B**), and consistency (mean diameter) were determined with a mini cone using the flow table method (**C**).

Regarding fresh mortars containing bismuth oxide (Figure 11A and Table 5), the results demonstrate that the incorporation of 5 wt% and 10 wt% Bi_2O_3 slightly increases τ_0 from 6.4 Pa for the control sample to 7.2 Pa and 7.4 Pa for Bi5 and Bi10, respectively. On the other hand, the plastic viscosity of Bi5 remained constant (i.e., approximately 1.06 Pa·s) compared to the value registered for the control sample (i.e., 1.03 Pa·s). Furthermore, increasing the Bi_2O_3 content to 10 wt% (i.e., Bi10) increased the plastic viscosity by 21% compared to that of the control sample. The direct correlation between the yield stress value and spread diameter of cementitious composites has been broadly reported in other literature findings [39,40]. The incorporation of Bi_2O_3 particles exhibited a negligible effect on the consistency of the composite, which agrees with the rheology results (Table 5). As shown in Figure 11C, the spread diameter of the control sample (i.e., 139 mm) slightly decreased and reached 134 mm and 133 mm for Bi5 and Bi10, respectively. The smaller size and hypersorbent nature of bismuth particles compared to the cement particles (Figure 1), which causes a lack of readily available free water at early ages, must be linked to the reduced workability of fresh mixes containing bismuth oxide particles. The results indicate that the deposition of silica coatings has an apparent effect on the rheology parameters of mixes containing Bi_2O_3 particles. The yield shear stress of the mixes is increased by adding Bi_2O_3 nanoparticles with both coating methods (i.e., method A and method B). However, the improvement in τ_0 seems to be more noticeable in mixtures containing aggregates

coated with method B, as aggregates coated with the method mentioned above exhibited a higher specific surface area and total volume of pores (see Table 2). The same trend was observed for the consistency of the mixtures. The consistency results indicate that the spread diameters of mixtures loaded with Bi_2O_3 particles and coated with method B, i.e., Bi5B and Bi10B, are lower than the values registered for their counterparts covered with particles coated with method A, by 5% and 4%, respectively.

As per Figure 11B and Table 5, the yield shear stress results showed that Gd5 and Gd10 (i.e., 6.4 Pa and 9.9 Pa, respectively) exhibited similar or higher values when compared to the value registered for the control sample (i.e., 6.4 Pa). As shown in the SEM images (Figure 6), the Gd_2O_3 particles tend to agglomerate and act as micron-sized particles. Due to the relatively low specific surface area (Table 2), the water absorption of Gd_2O_3 particles in Gd5 was limited. However, the increase in τ_0 of Gd10 has to be attributed to the relatively higher number of entrapped water molecules within the Gd_2O_3 agglomerates, which reduces the available water in the mixture. The consistency results also indicated an increase in the spread diameter of the Gd5 and Gd10 mixtures by approximately 6% and 7%, respectively, compared to the control mixture. However, due to the low accuracy of the mini-cone test, the difference between the spread diameter of G5 and G10 can be considered negligible.

The τ_0 of the mixtures containing 5 wt% silica-coated Gd_2O_3 particles increased. τ_0 increased from 6.4 Pa in Gd5 to 9.2 Pa and 10.3 Pa in Gd5A and Gd5B, respectively. The consistency results exhibited the same trend, as the spread diameters of Gd5A and Gd5B were lower than that of the G5 mixture by approximately 8% and 17%, respectively. In contrast, the yield shear stress of the Gd10 mixture was considerably diminished following the deposition of silica coatings on their surfaces. Due to the propensity of gadolinium oxide particles to cluster (Figure 6) together with the tendency of silicate particles to agglomerate [41], applying coating methods results in the production of micron-sized coated particles with a low specific surface area, which leaves more available water in the mixture; hence, this reducing the yield shear stress. In the Gd10 mixture, coating method B provides a higher τ_0 when compared to the corresponding value registered for method A. In this regard, the τ_0 of Gd10B is 31% higher than that of Gd10A. The same trend was recorded in the plastic viscosity values, where η_p of the mix containing coated particles employing method B (i.e., Gd10B) increased to 1.9 Pa·s, which is relatively higher than the value recorded for its coated counterpart employing method A (i.e., Gd10A). It should be noted that the mini-cone test (see Figure 11C) also demonstrated an increased spread diameter for all mixtures containing 10 wt% gadolinium oxide with and without coatings compared to that of the control samples.

4.4. Mechanical Performance

The compressive strength of cementitious composites was evaluated after 1 d, 2 d, 7 d, and 28 d of curing and is presented in Figure 12.

As shown in Figure 12A, at 2 days and 7 days of curing, all Bi_2O_3-modified mixtures displayed compressive strength values marginally lower than those of the control sample. However, increasing the replacement ratio from 5 wt% to 10 wt% negatively affects the mechanical performance of the mixtures. The results indicated that the effect of bismuth oxide incorporation and coatings is more evident after the first day of curing, in which the compressive strengths of the Bi5 and Bi10 mixtures are 84% and 91% lower the compressive strength of the control sample. The effect has to be associated with the considerable delay in the hydration process as a result of binder replacement, as verified in Section 4.2. The results indicated that the compressive strength of the mixtures increased following the coatings. For samples containing 5 wt% bismuth oxide, the compressive strength increased from 2.5 MPa for Bi5 to 7.1 MPa and 6.2 MPa for Bi5A and Bi5B, respectively. Similarly, for the samples containing 10 wt% bismuth oxide, the compressive strength increased from 1.6 MPa for Bi10 to 5.2 MPa and 5.1 MPa for Bi10A and Bi10B, respectively. From the second day of curing, the discrepancy between samples tends to decrease. After 28 d

of curing, the compressive strength of the mixtures containing bismuth oxide increased compared to that of the control sample. As shown in Figure 12A, the compressive strength increased from 58.1 MPa for the control sample to 67.6 MPa and 64.4 MPa for the B5 and B10 mixes, respectively. The enhancement in compressive strength must be associated with the filling effect induced by the presence of Bi_2O_3 particles in the cementitious matrix [15]. The presence of coating layers for the samples containing 5 wt% bismuth oxide is negligible. However, for samples with 10 wt% bismuth oxide, coating method B exhibited a slightly higher effect on mechanical performance than method A.
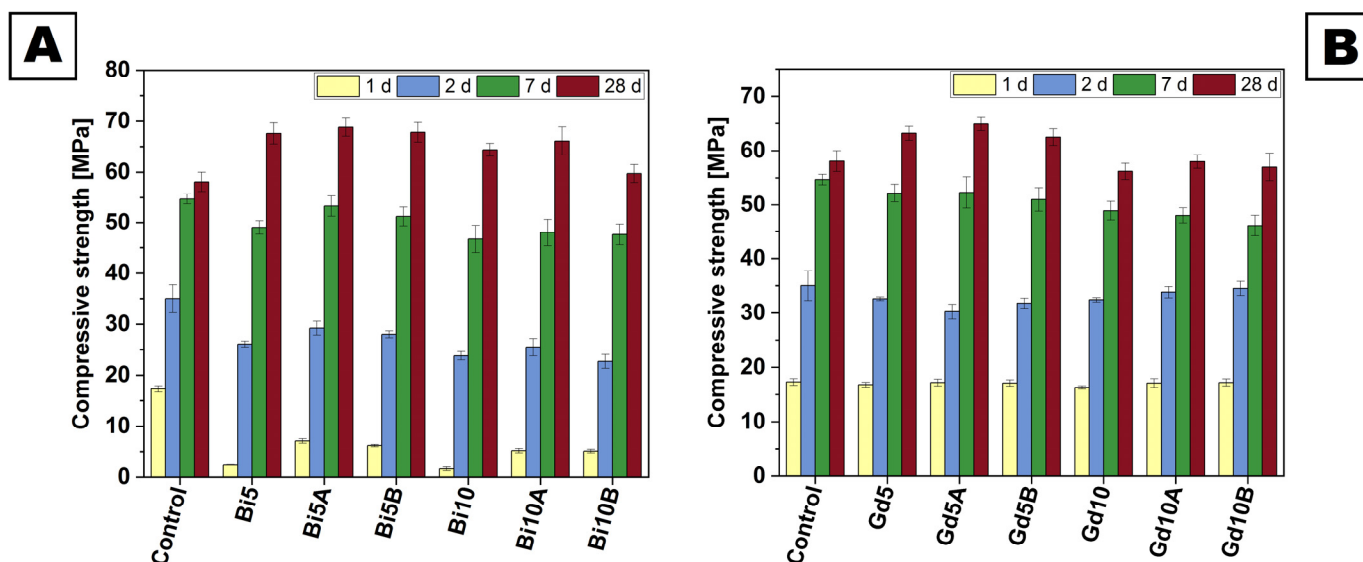

Figure 12. Compressive strength development of cement pastes containing Bi_2O_3 (**A**) and Gd_2O_3 (**B**) particles.

For all the mixtures containing gadolinium oxide particles (see Figure 12B) after 1 d, 2 d, and 7 d of curing, the effects of binder replacement and coatings on the compressive strength of the mixtures were negligible, as no statistically meaningful differences were observed. The slight reduction in compressive strength at early ages must be associated with the slight delay in the hydration process of the mixtures mentioned above. Piotrowski et al. also reported a delay in the hydration process and a slight compressive strength loss after the incorporation of Gd_2O_3 as an additive at early ages [38]. After 28 d of curing, enhancement in the compressive strength occurred for the samples containing 5 wt% gadolinium oxide particles. However, the results for samples with 10 wt% gadolinium oxide particles were comparable to the value recorded for the control sample. The highest compressive strength enhancement was registered for the Gd5A mixture, which is 12% higher than the value reported for the control sample.

Therefore, based on the compressive strength result, it can be concluded that due to substantial retardation of the hydration process, cement pastes containing Bi_2O_3 particles exhibit low strength development, especially in the first 48 h of hydration. However, after 28 d, substantially higher mechanical performance was reported for the Bi5 and Bi10 samples than for the control. In a previous study by Sikora et al. [15], cement pastes containing 10 wt% Bi_2O_3 exhibited lower mechanical performance than the control sample, which is attributed to the fact that no sonication was applied to Bi_2O_3 nanoparticles prior to addition. In this study, 10 min of ultrasonication was applied to deagglomerate the material and improve its nanofilling performance. The coating of Bi_2O_3 particles with silica exhibited marked effects on the acceleration of early strength development in favor of coating method A, with an almost threefold higher 1 d strength when compared to Bi5. This phenomenon is in line with the calorimetry study confirming the substantially accelerated hydration process of cementitious systems containing silica-coated Bi_2O_3 nanoparticles

(Section 4.2). In contrast, silica coating of coarser Gd_2O_3 microsized particles exhibited a relatively marginal effect on the strength development of cement pastes. It is worth noting that the inclusion of 5 wt% pristine Gd_2O_3 (Gd5) exhibited a beneficial effect on the mechanical performance of cement pastes after 28 d of curing, while samples containing 10 wt% (Gd10) exhibited comparable mechanical performance to that of the control sample.

5. Conclusions

Based on the results presented in this work, the following conclusions can be drawn:

- Two methods (A and B) of silica coatings of Bi_2O_3 and Gd_2O_3 particles were proposed. Both coatings differ from each other in terms of coating structure, thickness, porosity, and surface area. Silica synthesized via method A shows higher reactivity than silica synthesized according to method B. The negative aspects of the synthesized silica shell are similar to those of fused silica, which the high porosity and surface area of the silica shell can compensate. In terms of silica shell cost and synthesis requirements, method B shows advantages in relation to time and cost reduction and synthesis procedure complexity.

- Fresh property evaluations, both rheology and mini-cone tests, were shown to be a practical tool for understanding the effect of nanoparticles within cementitious composites. Including nanoparticles in the mixtures induced a noticeable thickening effect, which increased the yield shear stress. The coating process employing method B exhibited a predominant thickening effect in all the combinations compared to method A.

- Bi_2O_3 nanoparticles were found to have a hindering effect on the cement hydration process, resulting in a substantially delayed exothermic peak occurrence as well as lower peak power. The retardation effect increased in relation to the amount of the Bi_2O_3 content. Silica coating of Bi_2O_3 nanoparticles enabled a remarkable reduction in the negative impact of the presence of Bi_2O_3 in the hydration process. The proposed solid silica coating (method A) was found to be more suitable than the silica coating obtained with method B for accelerating the hydration process of cementitious systems containing Bi_2O_3 nanoparticles.

- Bi_2O_3 particles were found to have a negative effect on the early strength development (1 d and 2 d), resulting in drastically lower compressive strength values than those reported for the control cement paste. However, after 28 d, samples containing 5 wt% Bi_2O_3 followed by 10 wt% Bi_2O_3 exhibited higher compressive strengths than the control paste. Both coating methods, in favor of method A, exhibited marked effects on accelerating the early strength development of composites. After 28 d, the effects of silica-coated Bi_2O_3 particles were comparable to those of pristine particles.

- Gd_2O_3 particles at 5 wt% and 10 wt% replacement levels were found to result in slight retardation of cement hydration; however, the total heat release after 12 h of hydration was higher than that of the control sample. At 168 h, the total heat emitted was similar to that of pristine paste. The silica coating had marginal effects on the hydration process, most likely due to the coarser (micron) particle size in comparison to Bi_2O_3. However, in the first 12 h of hydration, cement pastes containing silica-coated Gd_2O_3 and using method B emitted a slightly higher amount of heat than pastes containing silica-coated Gd_2O_3 produced with method A.

- The presence of Gd_2O_3 in the cementitious system did not noticeably affect the early strength development of cement pastes. After 28 d of curing, pastes containing 5 wt% replacement of cement with Gd_2O_3 exhibited higher mechanical performance, while samples containing 10 wt% of Gd_2O_3 had minimally lower compressive strength than the control sample. The coating of Gd_2O_3 exhibited a negligible effect on the mechanical performance of cement pastes regardless of the synthesis method.

Supplementary Materials: The following supporting information can be downloaded at: https://www.mdpi.com/article/10.3390/coatings13101698/s1, Figure S1: Schematic representation of mini-cone geometry; Figure S2: The lattice planes of bismuth oxide (A) and gadolinium oxide (B); Figure S3: TEM images of silica particles synthesized via method B; Figure S4: Images of post-synthesis dry silica materials after evaporation (A): method A (left), method B (right), and images of post-synthesis solutions silica via method A (B) and method-B (C); Figure S5: Raman spectra of silica materials synthesized according to the method A and method B, using laser 830 nm.

Author Contributions: Conceptualization, K.C., M.C. and P.S.; methodology, K.C., T.K., M.S., E.M. and P.S.; validation, K.C., K.F., M.T., M.C., T.K., M.S., E.M. and P.S.; formal analysis, K.C., K.F., M.T., M.C., T.K., M.S., E.M. and P.S.; investigation, K.C., K.F., M.T., T.K. and P.S.; resources, E.M. and P.S.; data curation, K.C., K.F., M.T., T.K. and P.S.; writing—original draft preparation, K.C., K.F., M.T., M.C., T.K. and P.S.; writing—review and editing, K.C., M.C., M.S., E.M. and P.S.; visualization, K.C., M.C., T.K. and P.S.; supervision, P.S. and E.M.; project administration, P.S.; funding acquisition, P.S. All authors have read and agreed to the published version of the manuscript.

Institutional Review Board Statement: Not applicable.

Informed Consent Statement: Not applicable.

Data Availability Statement: The datasets generated and/or analyzed during this study are available from the corresponding author upon reasonable request.

Conflicts of Interest: The authors declare no conflict of interest.

References

1. Grazziotin-Soares, R.; Nekoofar, M.H.; Davies, T.E.; Bafail, A.; Alhaddar, E.; Hübler, R.; Busato, A.L.S.; Dummer, P.M.H. Effect of bismuth oxide on white mineral trioxide aggregate: Chemical characterization and physical properties. *Int. Endod. J.* **2014**, *47*, 520–533. [CrossRef] [PubMed]
2. Li, Q.; Coleman, N.J. The hydration chemistry of ProRoot MTA. *Dent. Mater. J.* **2015**, *34*, 458–465. [CrossRef] [PubMed]
3. Li, Q.; Coleman, N.J. Impact of Bi_2O_3 and ZrO_2 Radiopacifiers on the Early Hydration and C–S–H Gel Structure of White Portland Cement. *J. Funct. Biomater.* **2019**, *10*, 46. [CrossRef] [PubMed]
4. Marciano, M.A.; Garcia, R.B.; Cavenago, B.C.; Minotti, P.G.; Midena, R.Z.; Guimares, B.M.; Ordinola-Zapata, R.; Duarte, M.A.H. Influence of bismuth oxide concentration on the pH level and biocompatibility of white Portland cement. *J. Appl. Oral Sci.* **2014**, *22*, 268–273. [CrossRef]
5. Restuccia, L.; Favero, A.; Jagdale, P.; Cavalot, G.; Ferro, G.A. Design of bismuth oxide nanoparticles as lightweight aggregate in cement composites against X-rays. *Mater. Des. Process. Commun.* **2019**, *1*, e34. [CrossRef]
6. Abdalsalam, A.H.; Şakar, E.; Kaky, K.M.; Mhareb, M.; Ceviz Şakar, B.; Sayyed, M.I.; Gürol, A. Investigation of gamma ray attenuation features of bismuth oxide nano powder reinforced high-density polyethylene matrix composites. *Radiat. Phys. Chem.* **2020**, *168*, 108537. [CrossRef]
7. Karabul, Y.; İçelli, O. The assessment of usage of epoxy based micro and nano-structured composites enriched with Bi_2O_3 and WO_3 particles for radiation shielding. *Results Phys.* **2021**, *26*, 104423. [CrossRef]
8. El-Khatib, A.M.; Hamada, M.S.; Alabsy, M.T.; Youssef, Y.M.; Elzaher, M.A.; Badawi, M.S.; Fayez-Hassan, M.; Kopatch, Y.N.; Ruskov, I.N.; Abbas, M.I. Fast and thermal neutrons attenuation through micro-sized and nano-sized CdO reinforced HDPE composites. *Radiat. Phys. Chem.* **2021**, *180*, 109245. [CrossRef]
9. Dezhampanah, S.; Nikbin, I.M.; Mehdipour, S.; Mohebbi, R.; Moghadam, H. Fiber- reinforced concrete containing nano—TiO_2 as a new gamma-ray radiation shielding materials. *J. Build. Eng.* **2021**, *44*, 102542. [CrossRef]
10. Nikbin, I.M.; Mohebbi, R.; Dezhampanah, S.; Mehdipour, S.; Mohammadi, R.; Nejat, T. Gamma ray shielding properties of heavy-weight concrete containing Nano-TiO_2. *Radiat. Phys. Chem.* **2019**, *162*, 157–167. [CrossRef]
11. Nikbin, I.; Mehdipour, S.; Dezhampanah, S.; Mohammadi, R.; Mohebbi, R.; Moghadam, H.; Sadrmomtazi, A. Effect of high temperature on mechanical and gamma ray shielding properties of concrete containing nano-TiO_2. *Radiat. Phys. Chem.* **2020**, *174*, 108967. [CrossRef]
12. Sikora, P.; El-Khayatt, A.M.; Saudi, H.A.; Liard, M.; Lootens, D.; Chung, S.-Y.; Woliński, P.; Abd Elrahman, M. Rheological, Mechanical, Microstructural and Radiation Shielding Properties of Cement Pastes Containing Magnetite (Fe_3O_4) Nanoparticles. *Int. J. Concr. Struct. Mater.* **2023**, *17*, 7. [CrossRef]
13. Florez, R.; Colorado, H.A.; Alajo, A.; Giraldo, C.H. The material characterization and gamma attenuation properties of Portland cement-Fe_3O_4 composites for potential dry cask applications. *Prog. Nucl. Energy* **2019**, *111*, 65–73. [CrossRef]

14. Tekin, H.O.; Sayyed, M.I.; Issa, S.A. Gamma radiation shielding properties of the hematite-serpentine concrete blended with WO_3 and Bi_2O_3 micro and nano particles using MCNPX code. *Radiat. Phys. Chem.* **2018**, *150*, 95–100. [CrossRef]

15. Sikora, P.; El-Khayatt, A.M.; Saudi, H.A.; Chung, S.-Y.; Stephan, D.; Abd Elrahman, M. Evaluation of the effects of bismuth oxide (Bi_2O_3) micro and nanoparticles on the mechanical, microstructural and γ-ray/neutron shielding properties of Portland cement pastes. *Constr. Build. Mater.* **2021**, *284*, 122758. [CrossRef]

16. Gouda, M.M.; El-Khatib, A.M.; Abbas, M.I.; Al-Balawi, S.M.; Alabsy, M.T. Gamma Attenuation Features of White Cement Mortars Reinforced by Micro/Nano Bi_2O_3 Particles. *Materials* **2023**, *16*, 1580. [CrossRef]

17. El-Nahal, M.A.; Elsafi, M.; Sayyed, M.I.; Khandaker, M.U.; Osman, H.; Elesawy, B.H.; Saleh, I.H.; Abbas, M.I. Understanding the Effect of Introducing Micro- and Nanoparticle Bismuth Oxide (Bi_2O_3) on the Gamma Ray Shielding Performance of Novel Concrete. *Materials* **2021**, *14*, 6487. [CrossRef]

18. Amin, M.; Hakamy, A.A.; Zeyad, A.M.; Tayeh, B.A.; Saad Agwa, I. Improving the brittle behavior of high-strength shielding concrete blended with lead oxide, bismuth oxide, and tungsten oxide nanoparticles against gamma ray. *Struct. Eng. Mech.* **2023**, *85*, 29–53. [CrossRef]

19. Singh, G.; Saini, B. Nanomaterial in cement industry: A brief review. *Innov. Infrastruct. Solut.* **2022**, *7*, 45. [CrossRef]

20. Sikora, P.; Chougan, M.; Cuevas, K.; Liebscher, M.; Mechtcherine, V.; Ghaffar, S.H.; Liard, M.; Lootens, D.; Krivenko, P.; Sanytsky, M.; et al. The effects of nano- and micro-sized additives on 3D printable cementitious and alkali-activated composites: A review. *Appl. Nanosci.* **2022**, *12*, 805–823. [CrossRef]

21. Abdelzaher, M.A.; Shehata, N. Hydration and synergistic features of nanosilica-blended high alkaline white cement pastes composites. *Appl. Nanosci.* **2022**, *12*, 1731–1746. [CrossRef]

22. Krivenko, P.V.; Sanytsky, M.; Kropyvnytska, T. The Effect of Nanosilica on the Early Strength of Alkali-Activated Portland Composite Cements. *Solid State Phenom.* **2019**, *296*, 21–26. [CrossRef]

23. Ślosarczyk, A.; Klapiszewska, I.; Klapiszewski, Ł. Influence of nanosilica and binary oxide systems on the selected physical and mechanical properties of cement composites. *Physicochem. Probl. Miner. Process.* **2022**, *58*, 144184. [CrossRef]

24. Singh, L.P.; Bhattacharyya, S.K.; Mishra, G.; Ahalawat, S. Functional role of cationic surfactant to control the nano size of silica powder. *Appl. Nanosci.* **2011**, *1*, 117–122. [CrossRef]

25. Horszczaruk, E.; Aleksandrzak, M.; Cendrowski, K.; Jędrzejewski, R.; Baranowska, J.; Mijowska, E. Mechanical properties cement based composites modified with nano-Fe_3O_4/SiO_2. *Constr. Build. Mater.* **2020**, *251*, 118945. [CrossRef]

26. Han, B.; Li, Z.; Zhang, L.; Zeng, S.; Yu, X.; Han, B.; Ou, J. Reactive powder concrete reinforced with nano SiO_2-coated TiO_2. *Constr. Build. Mater.* **2017**, *148*, 104–112. [CrossRef]

27. Stynoski, P.; Mondal, P.; Wotring, E.; Marsh, C. Characterization of silica-functionalized carbon nanotubes dispersed in water. *J. Nanopart. Res.* **2013**, *15*, 1396. [CrossRef]

28. Sikora, P.; Abd Elrahman, M.; Chung, S.-Y.; Cendrowski, K.; Mijowska, E.; Stephan, D. Mechanical and microstructural properties of cement pastes containing carbon nanotubes and carbon nanotube-silica core-shell structures, exposed to elevated temperature. *Cem. Concr. Compos.* **2019**, *95*, 193–204. [CrossRef]

29. Pi, Z.; Xiao, H.; Liu, R.; Li, H. Combination usage of nano-SiO_2-coated steel fiber and silica fume and its improvement effect on SFRCC. *Compos. Part B Eng.* **2021**, *221*, 109022. [CrossRef]

30. Stöber, W.; Fink, A.; Bohn, E. Controlled growth of monodisperse silica spheres in the micron size range. *J. Colloid Interface Sci.* **1968**, *26*, 62–69. [CrossRef]

31. Suo, Y.; Guo, R.; Xia, H.; Yang, Y.; Yan, F.; Ma, Q. Study on modification mechanism of workability and mechanical properties for graphene oxide-reinforced cement composite. *Nanomater. Nanotechnol.* **2020**, *10*, 184798042091260. [CrossRef]

32. Haist, M.; Link, J.; Nicia, D.; Leinitz, S.; Baumert, C.; von Bronk, T.; Cotardo, D.; Eslami Pirharati, M.; Fataei, S.; Garrecht, H.; et al. Interlaboratory study on rheological properties of cement pastes and reference substances: Comparability of measurements performed with different rheometers and measurement geometries. *Mater. Struct.* **2020**, *53*, 92. [CrossRef]

33. Cendrowski, K.; Sikora, P.; Zielinska, B.; Horszczaruk, E.; Mijowska, E. Chemical and thermal stability of core-shelled magnetite nanoparticles and solid silica. *Appl. Surf. Sci.* **2017**, *407*, 391–397. [CrossRef]

34. Cendrowski, K.; Sikora, P.; Horszczaruk, E.; Mijowska, E. Waste-free synthesis of silica nanospheres and silica nanocoatings from recycled ethanol–ammonium solution. *Chem. Pap.* **2017**, *71*, 841–848. [CrossRef]

35. Cendrowski, K.; Chen, X.; Zielinska, B.; Kalenczuk, R.J.; Rümmeli, M.H.; Büchner, B.; Klingeler, R.; Borowiak-Palen, E. Synthesis, characterization, and photocatalytic properties of core/shell mesoporous silica nanospheres supporting nanocrystalline titania. *J. Nanopart. Res.* **2011**, *13*, 5899–5908. [CrossRef]

36. Yun, K.K.; Kim, J.B.; Song, C.S.; Hossain, M.S.; Han, S. Rheological Behavior of High-Performance Shotcrete Mixtures Containing Colloidal Silica and Silica Fume Using the Bingham Model. *Materials* **2022**, *15*, 428. [CrossRef]

37. Graf, C. Silica, Amorphous. In *Kirk-Othmer Encyclopedia of Chemical Technology*; John Wiley & Sons, Inc.: Hoboken, NJ, USA, 2000; pp. 1–43, ISBN 0471238961.

38. Piotrowski, T.; Glinicka, J.; Glinicki, M.A.; Prochoń, P. Influence of gadolinium oxide and ulexite on cement hydration and technical properties of mortars for neutron radiation shielding purposes. *Constr. Build. Mater.* **2019**, *195*, 583–589. [CrossRef]

39. Li, W.; Guo, L.; Liu, G.; Pan, A.; Zhang, T. Analytical and experimental investigation of the relationship between spread and yield stress in the mini-cone test for cemented tailings backfill. *Constr. Build. Mater.* **2020**, *260*, 119770. [CrossRef]

40. Tan, Z.; Bernal, S.A.; Provis, J.L. Reproducible mini-slump test procedure for measuring the yield stress of cementitious pastes. *Mater. Struct.* **2017**, *50*, 235. [CrossRef]
41. Liu, B.; Zhou, H.; Meng, H.; Pan, G.; Li, D. Fresh properties, rheological behavior and structural evolution of cement pastes optimized using highly dispersed in situ controllably grown Nano-SiO$_2$. *Cem. Concr. Compos.* **2023**, *135*, 104828. [CrossRef]